



Stress analysis of blade Rheometry by DEM simulations

Wenguang Nan^{*}, Yiqing Gu

School of Mechanical and Power Engineering, Nanjing Tech University, Nanjing 211816, China

ARTICLE INFO

Article history:

Received 4 June 2020

Received in revised form 7 August 2020

Accepted 9 August 2020

Available online 12 August 2020

Keywords:

DEM

Blade Rheometer

Mohr-coulomb

Wall friction

Passive failure

Shear stress

ABSTRACT

Blade rheometer has been used to characterise the rheological behaviour of bulk particles at high shear strain rate under dynamic conditions, yet little is known about its underlying powder mechanics. We analyse the effects of the shape and rotation direction of the blade, particle-blade friction and particle aspect ratio on the rheological behaviour of bulk particles in the blade rheometer by using DEM simulations. The shear stress arising in front of blade increases linearly with the radial position, and it is sensitive to the rotation direction and wall friction of the twisted blade. The sensitivity of blade torque to the shape and wall friction of the blade is depicted from a model proposed in this work, i.e. a vertical retaining wall supporting granular material in passive failure. The blade torque correlates well with the shear stress, and a mathematic model is proposed to quantify the linear relationship between them.

© 2020 Elsevier B.V. All rights reserved.

1. Introduction

Particulate solids have been widely used in various industrial engineering, such as minerals, coal plant and additive manufacturing. The processing of particulate solids is sensitive to bulk powder properties and environmental conditions, making the prediction of powder flow highly desirable. Several techniques have been established for characterising bulk powder failure for flow initiation, such as Schulze Ring Shear Tester [1] and Sevilla Powder Tester [2]. These testers produce different parameters to quantify bulk powder properties, which could be applied to the design of hopper. Beyond the flow initiation, the prediction of bulk rheological properties in dynamic conditions is more desirable in real manufacturing process, such as mixing and die filling, and the bulk parameters are sensitive to shear strain rate, but there are no quasi-static based approaches that can characterise the bulk parameters at high strain rates.

Rheometry and modelling of powder behaviour in the rheometer working at dynamic flow conditions have received some attention in recent years, which was recently reviewed by Ghadiri et al. [3]. Tardos and co-workers [4–7] analysed the particle flow inside a Couette device consisting of two co-axial vertical cylinders, in which the particles are sheared in the annular gap and shear stress is calculated from the torque on the rotating inner cylinder. The Couette rheometer can be operated in ‘batch’ model (no axial flow) or ‘continuous’ mode (with downward axial flow), and their results showed that the shear stress in the latter was sensitive to the shear strain rate and the particle flow could transit from quasi-static to intermediate regimes. However, the recent work of

Gutam et al. [8] and Kumar et al. [9] found that the flow pattern in the Couette rheometer was more complex than previously perceived due to the secondary recirculating flow. Lupo et al. [10] also argued that Couette rheometer did not reliably estimate the effective angle of internal friction, as it was strongly affected by the small experimental error in the torque measurement. As an alternative to Couette device, a rotating blade has been used to study powder's dynamic response to shear deformation, such as FT4 Rheometer of Freeman Technology [11], powder cell of Anton Paar Modular Compact Rheometer [12] or the rheometer with a blade rotating at a fixed height inside the particle bed [13–15]. In the former, a twisted blade usually rotates anti-clockwise while moving downward into the particle bed. As the shear stress is not measured or calculated in these rheometers, it is necessary to analyse the underlying mechanics of powder flow induced by the blade and relate the measured parameters (i.e. blade torque and force) to the bulk powder rheological characteristics. Bruni et al. [13,14], Tomasetta et al. [15] and Salehi et al. [16] analysed the rheological behaviour of aerated and non-aerated powder in the rheometer with a rotating plane blade. For the rheometer working at very slow rotational speed (<1 rpm), they proposed a rheological model to predict the internal frictional angle of bulk powder from the measured blade torque, in which the particles enclosed by the blade tip were assumed to be a rigid body without shearing. Salehi et al. [12] compared torque measurements between different impeller geometries (i.e. cylindrical and circular shapes, and two-blade impellers) in Anton Paar powder cell by DEM simulation, and the difference was attributed to different shearing surfaces. Hare et al. [17], Nan et al. [18–20] and Vivacqua et al. [21] have carried out a systematic study of the effects of cohesion, air drag and strain rate, and particle shape on particle flow in the FT4 rheometer by analysing the stress and strain fields of bulk particles. They identified that the flow energy

^{*} Corresponding author.

E-mail address: nanwg@njtech.edu.cn (W. Nan).

(i.e. input work required to drive the rotating blade into the powder bed) correlated well with the particle stress in front of the blade, but no direct physical models were consistently found for the relationship between the blade torque and bulk rheological properties.

We report on our analysis of the rheological behaviour of particle flow sheared by a rotating blade using numerical simulations with discrete element method (DEM). The effects of the shape and rotation direction of the blade, blade roughness and particle aspect ratio on the particle stress and blade torque have been analysed, and a rheological model is proposed to quantify the relationship between the particle stress in front of the blade and blade torque. This provides a step towards understanding the underlying dynamics of blade powder rheometer.

2. Method

In the blade powder rheometer, a twisted or plane blade rotates at a fixed vertical position in a cylinder vessel, which is filled up with particles, as shown in Fig. 1. The particle dynamics in the rheometer are simulated by DEM, where the particles are modelled as discrete phases and their motions are tracked individually by solving Newton's laws of motion [22,23], for which the EDEM™ software package provided by DEM Solutions, Edinburgh, UK, is used:

$$m_i \frac{d\mathbf{v}_i}{dt} = \sum \mathbf{F}_{c,i} + m_i \mathbf{g} \quad (1)$$

$$\frac{d(\mathbf{I}_i \cdot \boldsymbol{\omega}_i)}{dt} = \mathbf{R}_i \cdot \sum \mathbf{M}_{c,i} \quad (2)$$

where m_i , \mathbf{I}_i , \mathbf{v}_i and $\boldsymbol{\omega}_i$ are the mass, moment of inertia, translational velocity and angular velocity, respectively; $\mathbf{F}_{c,i}$ is the contact force, originating from particle interactions with neighbouring particles or wall; $\mathbf{M}_{c,i}$ is the contact torque, arising from the tangential and normal contact force as well as rolling friction; \mathbf{R}_i is the rotation matrix from the global to the local coordinate system. In this work, the rodlike particle is used, which is described by the overlapping multi-sphere model [24], as shown in Fig. 1 and Fig. 2. There are no inter-sphere forces between the spherical elements in the same rod. The aspect ratio AR is defined as the ratio of the length L of cylinder part to the diameter $d = 2R$, and it is reduced to 0 for spheres. Obviously, the difference between the real rod and one represented by the clumped spheres can be adjusted by controlling the separation distance fraction of neighbouring spheres ($\delta = x/d$, the ratio of the normal overlap of two adjacent spheres to the diameter of the rod). Generally, $\delta = 0.5$ is sufficiently large to give an accurate representation of the real rod, while providing reasonable computational time, as suggested by Grof et al. [25,26] and Nan et al.

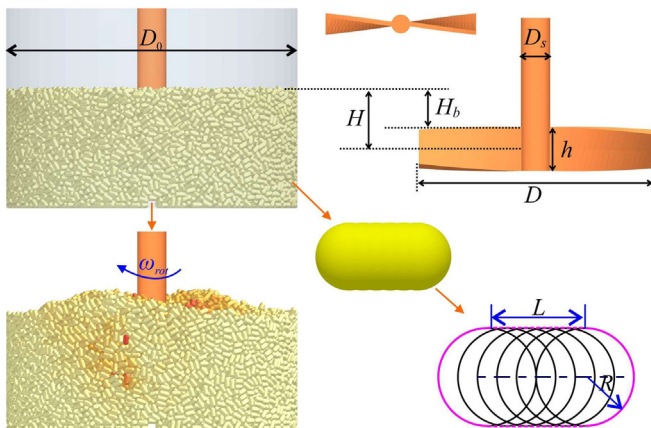


Fig. 1. Schematic diagram of simulation set-up for blade powder rheometer.

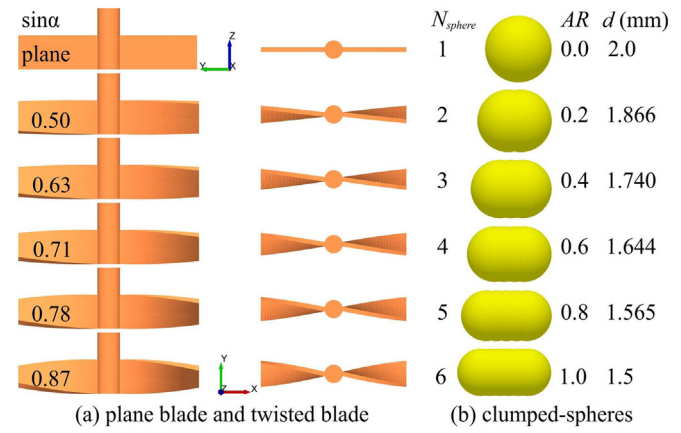


Fig. 2. Blade shape and rodlike particles described by clumped-spheres.

[27]. As the aspect ratio of rod in this work varies from 0 to 1.0 with an increment step of 0.2, a larger ratio (i.e. $\delta = 0.8$) is used, resulting in the number of clumped-spheres of an individual rod being $N_{sphere} = 5AR + 1$. Thus, one increment step of aspect ratio corresponds to one more sphere needed to be clumped within an individual rod. For the interaction of rod-wall and rod-rod, the elastic contact force is described by Hertz-Mindlin contact model. More features and further information of the contact model are given by Thornton [23], which are not shown here for brevity.

The diameters of the blade and vessel are $D = 64$ mm and $D_0 = 80$ mm, respectively. The height of the blade is $h = 12$ mm and the diameter of the shaft is $D_s = 8$ mm. The thickness of the blade is 2 mm. The blade is first fixed above the rough base with a distance of 8 mm between the blade bottom and base. A packed bed with a height of about 46 mm is generated by using the poured packing method where the orientation of the rodlike particles is randomly generated, and then it is agitated by the rotational motion of the blade after removing the particles above the pre-set height, where the rotational speed of the blade is 30 RPM (i.e. tip speed of 0.1 m/s). The blade first accelerates in 0.1 s and then rotates at the pre-set constant speed, and the torque of the blade is monitored. In the standard case, a blade with a twist angle of 39° ($\sin \alpha = 0.63$) and ceramic particles with $d = 1.5$ mm and $L = 1.5$ mm [28] (i.e. volume-equivalent sphere diameter $d_v = 2.0$ mm) are used; the particles above the height of 32 mm are removed to generate an over-burden depth $H_b = 12$ mm before the rotation of the blade. The material properties and interaction parameters in the simulations are listed in Table 1 and Table 2, respectively.

To explore the effects of blade geometry on the particle dynamics, the rheometer with plane blade and twisted blade of different twist angle are compared, i.e. $\sin \alpha = 0, 0.5, 0.63, 0.71, 0.78, 0.87$ (namely, $\alpha = 0^\circ, 30^\circ, 39^\circ, 45^\circ, 51^\circ$ and 60° , respectively), as shown in Fig. 2. The twisted blade can rotate in anti-clockwise or clockwise directions. The effect of blade roughness on the blade torque is explored by using different particle-blade friction coefficient, i.e. 0.0, 0.1, 0.35, 0.5, 0.8. Besides the blade shape and blade roughness, the particles with different aspect ratio are also used to investigate the sensitivity of rheological behaviour to particle shape, i.e. $AR = 0, 0.2, 0.4, 0.6, 0.8$ and 1.0, as shown in Fig. 2, where the volume-equivalent sphere diameter is $d_v = 2.0$ mm.

Table 1
Material properties in simulations.

Material property	Particles	Blade
Density, ρ (kg/m ³)	3300	7800
Shear modulus, G (Pa)	1×10^8	7.3×10^{10}
Poisson ratio, ν	0.3	0.3

Table 2
Contact interaction parameters in simulations.

Interaction property	Particles-particle	Particle-blade
Friction coefficient, μ	0.5	0.35
Rolling friction coefficient, μ_r	0.01	0.01
Restitution coefficient, e	0.6	0.6

If not specified, the simulation conditions and particle properties in the simulations below are the same as the corresponding ones in the standard case, i.e. over-burden depth $H_b = 12$ mm, particle-blade friction of 0.35, aspect ratio $AR = 1.0$, twist angle of $\sin \alpha = 0.63$.

3. Simulation results

3.1. Stresses analysis

As the blade agitates the particle bed, the particles close to the blade is sheared, whilst particles remote from the blade are essentially stationary. Thus, the stress analysis is conducted for the particles immediately in front of the blade. Four uniform measurement cells along the radial direction of each side of the blade are used, which are in blue, green, magenta and red colour, respectively, as shown in Fig. 3. The circumferential depth (θ direction) of the measurement cell is $l = 6$ mm, i.e. $3d_v$, which is in the range of the shear band [17–20,29,30]. The height (z direction) of the measurement cell is the same as the blade, and the radial size (r direction) of the measurement cell is $(R-R_s)/4$, i.e. 7 mm. The stress tensor of bulk particle flow is given as:

$$\sigma_{ij} = \frac{1}{V} \left(\sum_{p \in V} m_p \delta v_i \delta v_j + \sum_{c \in V} f_{ij} r_{ij} \right) \quad (3)$$

where V is the cell volume; m_p is the mass of particle p ; δv_i and δv_j are the fluctuation velocities of particle p ; f_{ij} is the contact force at contact c and r_{ij} is the corresponding branch vector between mass centre of particle i and that of particle j . Based on the stress tensor, three principal stresses could be calculated: major one σ_1 , intermediate one σ_2 and minor one σ_3 . According to the friction law, the yield state of bulk particle flow could be described by Mohr-Coulomb criterion [31], where the intermediate principal stress σ_2 is assumed to play no role, as shown in Fig. 4. The normal stress σ and shear stress τ are given as:

$$\sigma = \frac{\sigma_1 + \sigma_3}{2} \quad (4)$$

$$\tau = \frac{\sigma_1 - \sigma_3}{2} \quad (5)$$

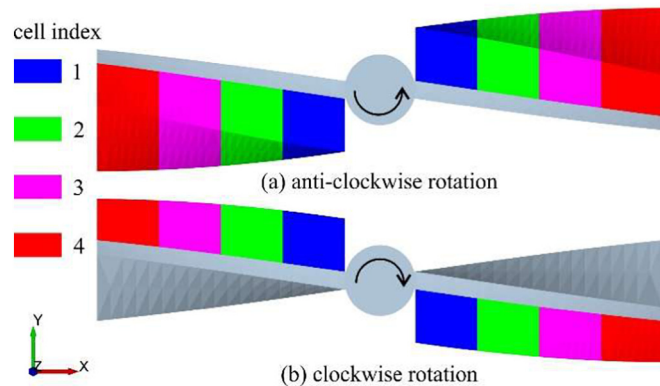


Fig. 3. Measurement cells with the same size for stress analysis in front of the blade in the moving direction of the blade, where the cells are partly hid in current perspective.

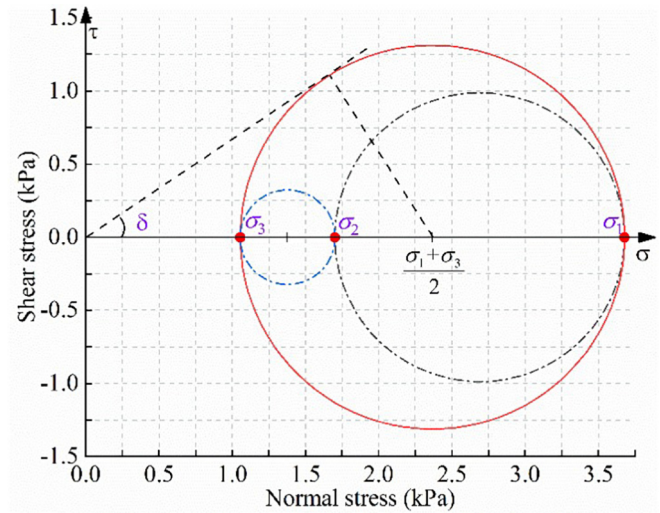


Fig. 4. The schematics of Mohr-Coulomb criterion in the standard case.

The bulk friction coefficient at the yield state is described by the linear relationship between the shear and normal stresses:

$$\sin \delta = \tau / \sigma \quad (6)$$

where δ is the effective angle of internal friction.

The blade shape has an important effect on the distribution of particle stress along the radial direction, as shown in Fig. 5, where cell 1 is closest to the shaft while cell 4 is most far away from the shaft, as shown in Fig. 3. For the plane blade, the shear stress increases linearly as the cell is far away from the shaft. In the cases of clockwise rotation of twisted blade, the rheometer works in an aggressive flow pattern causing stronger compression. Thus, larger shear stress could be obtained in all cells than that of plane blade. The shear stress also shows a linear increase with the radial position of the cell. In the cases of anti-clockwise rotation of twisted blade, the rheometer works in a gentle flow pattern, and the shear stress is much reduced in all cells, especially for the cells far away from the shaft, compared to that of plane blade. As $\sin \alpha$ increases to 0.63, a uniform distribution of shear stresses in cells 2–4 could be obtained, indicating that the twisted blade shears the particle bed almost uniformly, which is preferred by the

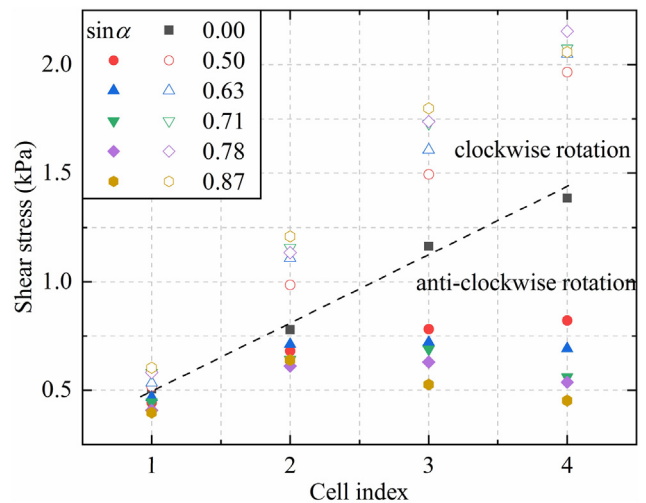


Fig. 5. Distribution of shear stress in the measurement cells along the radial direction of the blade.

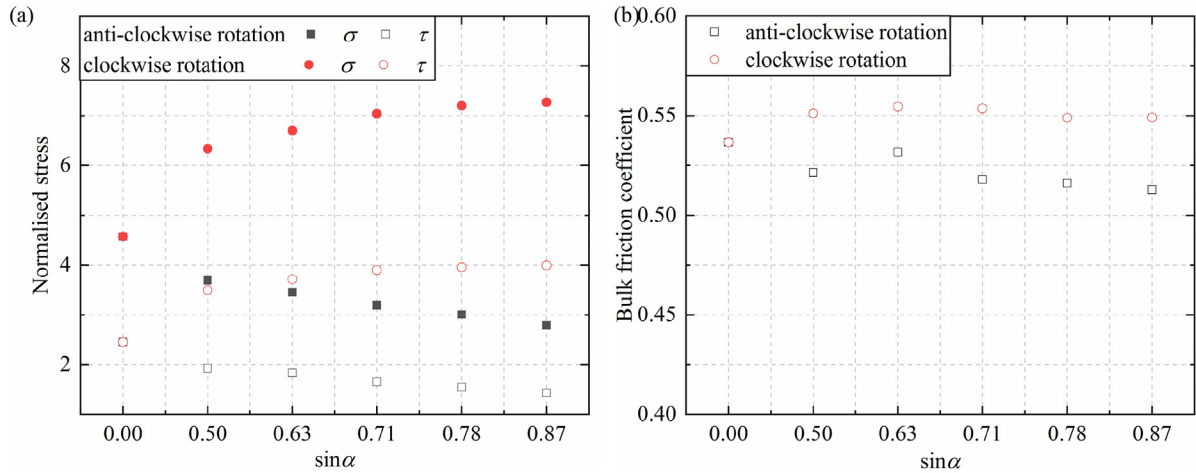


Fig. 6. Effect of the shape and rotation direction of blade on (a) cell-averaged normal and shear stresses (normalised by γH) and (b) bulk friction coefficient.

conditioning process. For $\sin\alpha$ larger than 0.63, the shear stress in cells 2–4 begins to decrease with the increase of the radial position of the cell. Fig. 5 also shows that the local shear stress close to blade tip is more affected by the shape and rotation direction of the blade.

Fig. 6 shows the averaged value of the normal and shear stresses as well as the bulk friction value in the measurement cells, where the stresses are normalised by the hydrostatic pressure γH ($\gamma = \rho_b g$ is the bulk weight density of the material). As the blade shape changes from plane to twist geometry, the normal stress shows a sharp increase when rotating clockwise and a dramatic decrease when rotating anti-clockwise. With further increase of the twist angle, the normal stress increases or decreases gradually to a plateau. Correspondingly, the shear stress is in the same trend of the normal stress with the increase of twist angle in all cases. Compared to the stress, the bulk friction coefficient is much less sensitive to the shape and rotation direction of the blade, which is intuitively expected. The bulk friction coefficient shows a little decrease in the case of anticlockwise rotation of blade, compared to the one of clockwise rotation of blade.

The surface roughness of the blade also affects the shear stress and bulk friction coefficient, as shown in Fig. 7, where the surface roughness is hypothetically described by the particle-blade friction coefficient.

With the increase of particle-blade friction coefficient, the shear stress in all cases first increases linearly, and then approaches to a plateau when particle-wall friction coefficient is larger than particle-particle friction coefficient (i.e. 0.5). The bulk friction coefficient is also sensitive to particle-wall friction coefficient, especially for small particle-wall friction coefficient. It suggests that the rheological behaviour of bulk particles in the rheometer is sensitive to the wall friction of the blade, especially for the blade with smooth surface. Fig. 7 also shows that the shape and rotation direction of the blade does not affect the trend of the variation of rheological parameters with the increase of particle-blade friction coefficient.

The rheological behaviour of bulk particles is sensitive to the physical properties of an individual particle, i.e. the aspect ratio of rodlike particle, as shown in Fig. 8. With the increase of particle aspect ratio, the shear stress increases due to stronger interlocking between particles, especially in the rheometer working in the aggressive mode (i.e. clockwise rotation of the blade). The difference of the shear stress between the cases of different blade shape and rotation direction is enlarged by larger particle aspect ratio. Similarly, the bulk friction coefficient also increases with particle aspect ratio. For spherical particles ($AR = 0$), the bulk friction coefficient is almost constant with the variation of the shape and rotation direction of the blade, i.e. 0.4, corresponding an

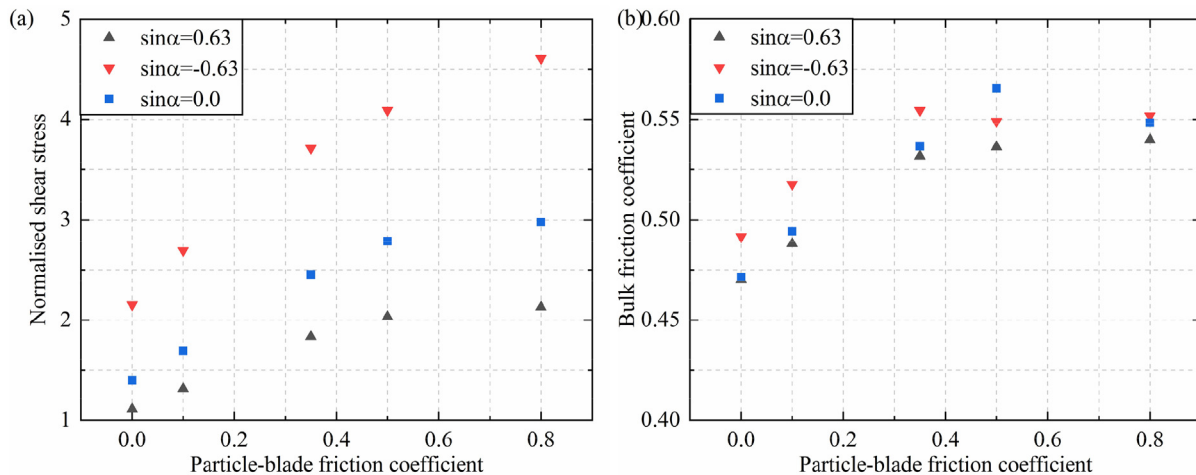


Fig. 7. Effect of particle-blade friction coefficient on (a) cell-averaged shear stress (normalised by γH) and (b) bulk friction coefficient, where $\sin\alpha = 0.63$ and -0.63 represent the anti-clockwise and clockwise rotations of twisted blade, respectively, and $\sin\alpha = 0$ represents the plane blade.

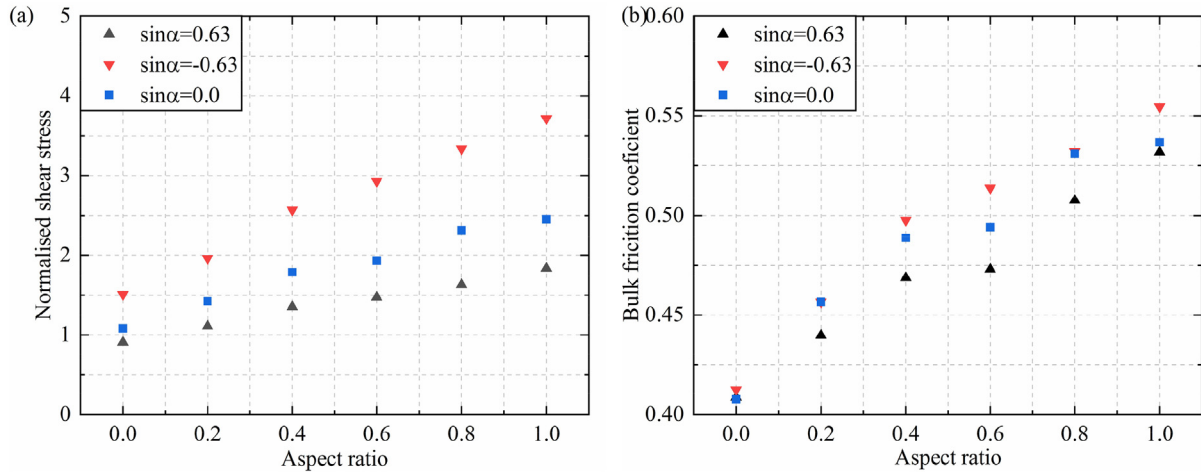


Fig. 8. Effect of particle aspect ratio on (a) cell-averaged shear stress (normalised by γH) and (b) bulk friction coefficient, where $\sin\alpha = 0.63$ and -0.63 represent the anti-clockwise and clockwise rotations of twisted blade, respectively, and $\sin\alpha = 0$ represents the plane blade.

internal friction angle of 24 deg. For rodlike particles, the bulk friction coefficient fluctuates a little between the cases of different shape and rotation direction of blade. This is also for the small fluctuations of bulk friction coefficient with the variation of the shape and rotation direction of the blade in Figs. 6–7, where rodlike particles with $AR = 1.0$ is used. It may be caused by the variation of interaction between the particle orientation and blade motion, which needs further investigation.

Besides the Mohr-Coulomb criterion used above, the Drucker-Prager criterion could also be used to describe the yield state of bulk particle flow, where the normal and shear stresses are given as [31]:

$$\sigma_{D-P} = \frac{\sigma_1 + \sigma_2 + \sigma_3}{3} \quad (7)$$

$$\tau_{D-P} = \frac{\sqrt{(\sigma_1 - \sigma_2)^2 + (\sigma_1 - \sigma_3)^2 + (\sigma_2 - \sigma_3)^2}}{\sqrt{6}} \quad (8)$$

Fig. 9 compares the stresses and bulk friction coefficient in Drucker-Prager criterion and Mohr-Coulomb criterion. Both criteria give the same shear stress with a deviation less than 5%, which is also true for

other cases in this work. Compared to Drucker-Prager criterion, the normal stress in Mohr-Coulomb criterion is a little larger, resulting in a smaller friction angle, i.e. $\sin\delta$ is about 10% less than $\sin\delta_{D-P}$. It suggests that at the same normal stress, Mohr-Coulomb criterion will give smaller yield shear stress, which is intuitively expected according to the theory of soil mechanisms.

3.2. Blade torque analysis

The variation of blade torque with blade shape, particle-blade friction coefficient, particle aspect ratio and over-burden depth is shown in Fig. 10. With the increase of twist angle of the blade, the blade torque shows a different trend in the anti-clockwise and clockwise rotations of the blade. The blade torque is also sensitive to the blade surface roughness, i.e. particle-wall friction coefficient. It increases linearly with the over-burden depth, and a larger blade torque could also be obtained for the particles with larger aspect ratio, which is intuitively expected.

To explain the sensitivity of the blade torque to the shape and rotation direction as well as surface roughness of the blade, a representative

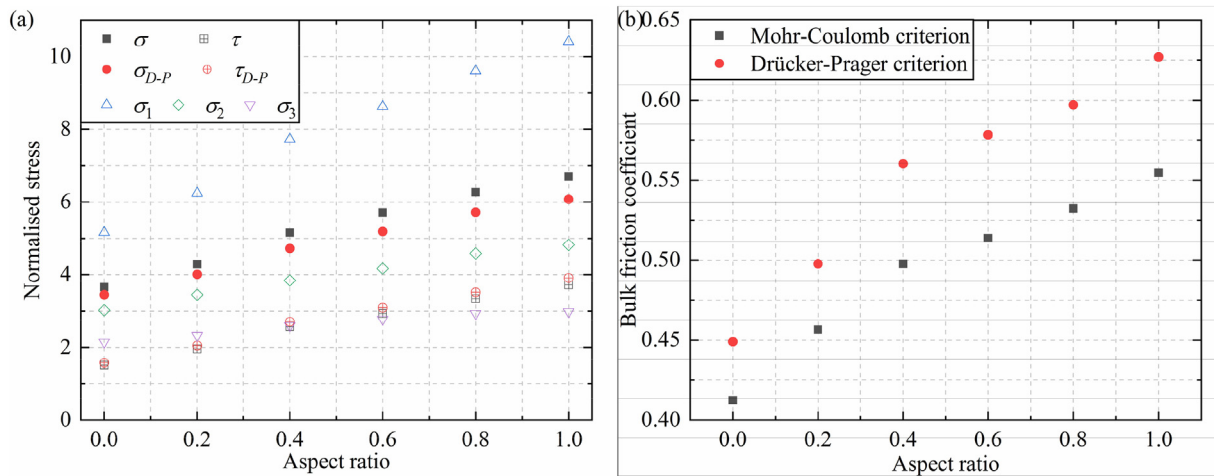


Fig. 9. Comparison between Drucker-Prager criterion and Mohr-Coulomb criterion for (a) cell-averaged stresses (normalised by γH) and (b) bulk friction coefficient with clockwise rotation of the twisted blade ($\sin\alpha = -0.63$).

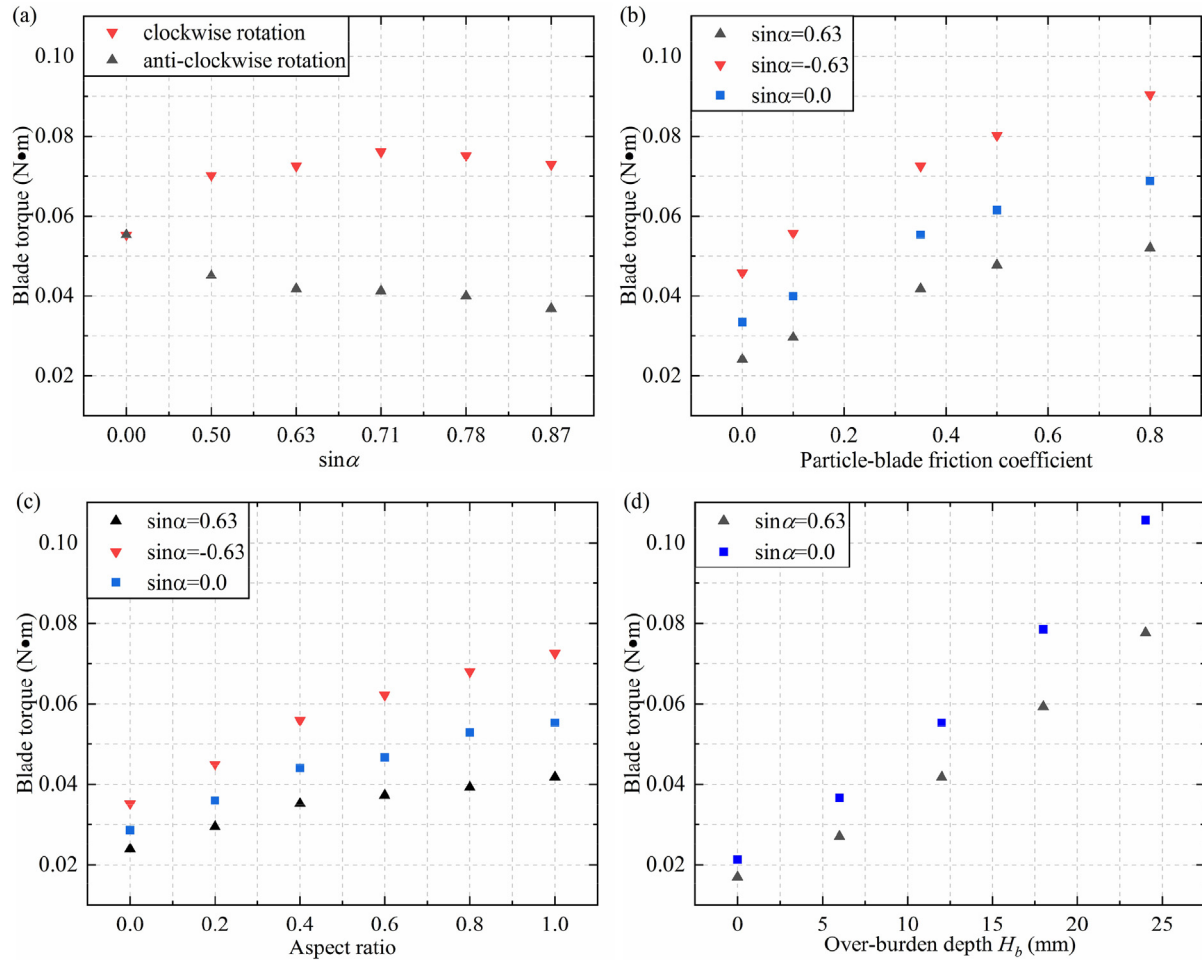


Fig. 10. Variation of blade torque with (a) shape and rotation direction of the blade, (b) particle-blade friction coefficient, (c) particle aspect ratio, and (d) over-burden depth.

slice (blue colour) of the blade is focused, i.e. r to $r + dr$, as shown in Fig. 11(a). The contribution of this slice to the blade torque is given as:

$$T = 2 \int_{D_s/2}^{D/2} dF_n \cdot r \quad (9)$$

For simplicity, the plane blade is firstly focused and the slice is first assumed to a vertical retaining wall supporting a cohesionless granular material in a passive failure, and a stress Q is applied to the horizontal top surface of the fill to consider the effect of particle weight above it and the reaction to the compression due to blade motion, as shown in

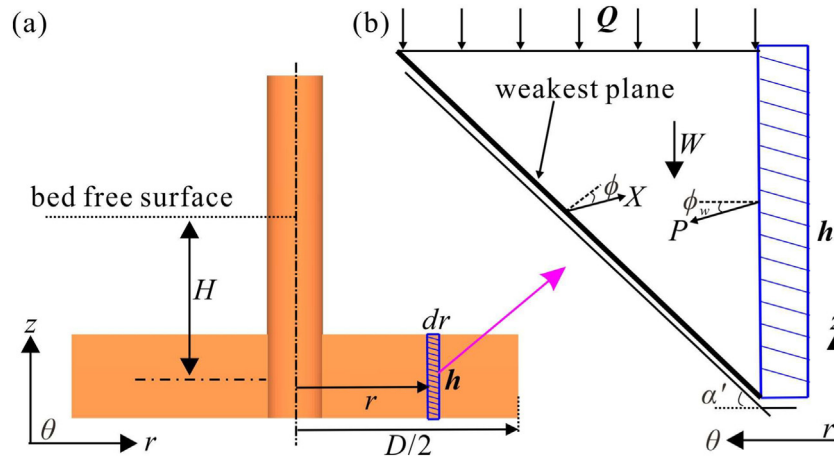


Fig. 11. Schematics of the Coulomb's method of wedges of the blade, (a) representative slice in blue colour; (b) the wedge of the sliding material in z - θ plane, which is subjected to resultant force X , the supporting force P from the passive failure of the retaining wall, and its own weight $W = \gamma h^2/2 \times \cot\alpha' \times dr$.

Fig. 11(b). By using Coulomb's method of wedge [32], the force balance could be given as:

$$P \cos \phi_w = X \sin(\alpha' + \phi) \quad (10)$$

$$X \cos(\alpha' + \phi) - P \sin \phi_w = \left(\frac{\gamma h^2}{2} + Q \right) h \cot \alpha' dr \quad (11)$$

where P is supporting force from the passive failure of the retaining wall; X is the resultant force on the slip plane; α' is the inclined angle of the slip plane; $\tan \phi$ is the bulk particle friction in Coulomb criterion; ϕ_w is the angle of wall friction, and it is limited by $\tan \phi_w \leq \tan \phi$. Thus, dF_n (i.e. in the circumferential direction, θ) on the slice could be given as:

$$dF_n = P \cos \phi_w = \left(\frac{\gamma h^2}{2} + Qh \right) f dr \quad (12)$$

$$f = \frac{\cot \alpha'}{\cot(\alpha' + \phi) - \tan \phi_w} \quad (13)$$

For passive failure, f has a minimum value with the variation of α' , given as:

$$f = \frac{\cos^2 \phi}{(1 - \sqrt{1 + \tan \phi_w / \tan \phi} \sin \phi)^2} \quad (14)$$

If the effect of the twist shape of the blade is considered, the inclined angle η is introduced, which is defined as the angle between the major orientation of the slice and the vertical direction. For example, for the slice shown in Fig. 11, its major orientation is in vertical direction, and thus the inclined angle is 0° . For the twisted blade, with the increase of its radial position r , the major orientation of the slice deviates more from the vertical direction, resulting in larger inclined angle. Meanwhile, for the blade with larger twist angle, the inclined angle of the slice at the same radial position is also larger. For the slice within a twisted blade, dF_n is then given as [32,33]:

$$dF_n = P \cos(\eta + \phi_w) = \left(\frac{\gamma h^2}{2} + Qh \right) f dr \quad (15)$$

$$f = \frac{\cos^2(\eta - \phi)}{\cos^2 \eta \left(1 - \sqrt{\frac{\sin(\phi + \phi_w) \sin \phi}{\cos(\eta + \phi_w) \cos \eta}} \right)^2} \quad (16)$$

Thus, the blade torque is given as:

$$T = 2 \int_{D/2}^{D/2} \left(\frac{\gamma h^2}{2} + Qh \right) f dr \quad (17)$$

where Q depend on the radial position r of the slice; f could be given by Eq. (14) for plane blade, and Eq. (16) for twisted blade which depends on r .

As the several parameters (i.e. f and Q) are unknown, it is not practical to predict blade torque from Eq. (17). However, according to above equations, it is distinct that the blade roughness (i.e. μ_w), blade shape (i.e. η) and rotation direction (i.e. plus or minus of η) could indeed influence the blade torque.

3.3. Models for blade powder rheometer

For the powder rheometer with a blade rotating at the fixed vertical position, Bruni et al. [13] proposed a rheological model to predict the blade torque through Mohr–Coulomb approach [32], and examined the model in their experiment by using a plane blade rotating very slowly (< 1 rpm). The shearing surface around the blade was assumed to shaped like the cylinder with a height h and diameter D equal to

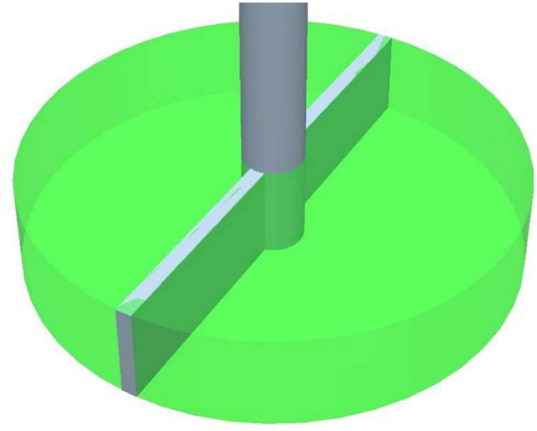


Fig. 12. The shearing surface assumed to shaped like the cylinder with a height and diameter equal to the ones of the blade in Bruni et al. [13], where the particles inside the cylinder were actually assumed to be a solid body without shearing inside.

the ones of the blade, as shown in Fig. 12, and the stress on the top/bottom surface was assumed uniform. Thus, the estimated resistant torque was the sum of the contributions of the stresses acting on the top, bottom and lateral surfaces of the shearing surface [13]:

$$T = \frac{\pi D^2}{6} \sigma_{zz} (D + 3hk) \tan \phi \quad (18)$$

where $\tan \phi$ is the bulk friction in Coulomb criterion, and is equal to $\sin \delta$ in Mohr criterion; $k = (1 - \sin \delta) / (1 + \sin \delta)$ corresponds to active state of stress, and $k = (1 + \sin \delta) / (1 - \sin \delta)$ corresponds to passive state of stress; σ_{zz} is the normal stress in the z direction, which could be estimated through Janssen's analysis [32]. For the penetration depth H smaller than the vessel diameter D_0 , σ_{zz} is simplified as:

$$\sigma_{zz} = \gamma H \quad (19)$$

where γ is the bulk weight density of the material. Thus, the resistant torque on the blade is given as:

$$T = \frac{\pi D^3}{6} \gamma H \times \beta \quad (20)$$

$$\beta = \left(1 + \frac{3h}{D} k \right) \sin \delta \quad (21)$$

To identify the state of shearing surface in the blade rheometer in this work, i.e. active or passive failure, the stress analysis is conducted for the cylinder in Fig. 12. As shown in Fig. 13, the vertical stress σ_{zz} is equal to the minor principal stress σ_3 in all cases, including plane and twisted blades, clockwise and anti-clockwise rotation of the blade, as well as the particles of different aspect ratio. Thus, β should be calculated based on the passive state of the shearing surface shown in Fig. 12, i.e. $k = (1 + \sin \delta) / (1 - \sin \delta)$. The predictions of β from the torque (Eq. (20)) and internal friction angle (Eq. (21)) are compared in Fig. 13. It could be found that the data points are scattered.

In the model (Eq. (18)), the particles enclosed by the two tips of the blade were assumed to be a rigid body without shearing. Thus, this model actually assumed the blade rotating the particle bed to be a rotating cylinder cell embedded in the particle bed. As a result, the sensitivity of blade torque to surface roughness and shape of the blade and the rotation direction of the twisted blade, as well as the non-uniform feature of the distribution of the stress on the top/bottom surface, were neither considered in the model. Actually, the shear stress on the top/bottom surface is non-uniform in radial direction, as shown in Fig. 5. Meanwhile, for the particles within the cylinder cell, only the ones close to the blade are strongly sheared, whilst others remote from the blade

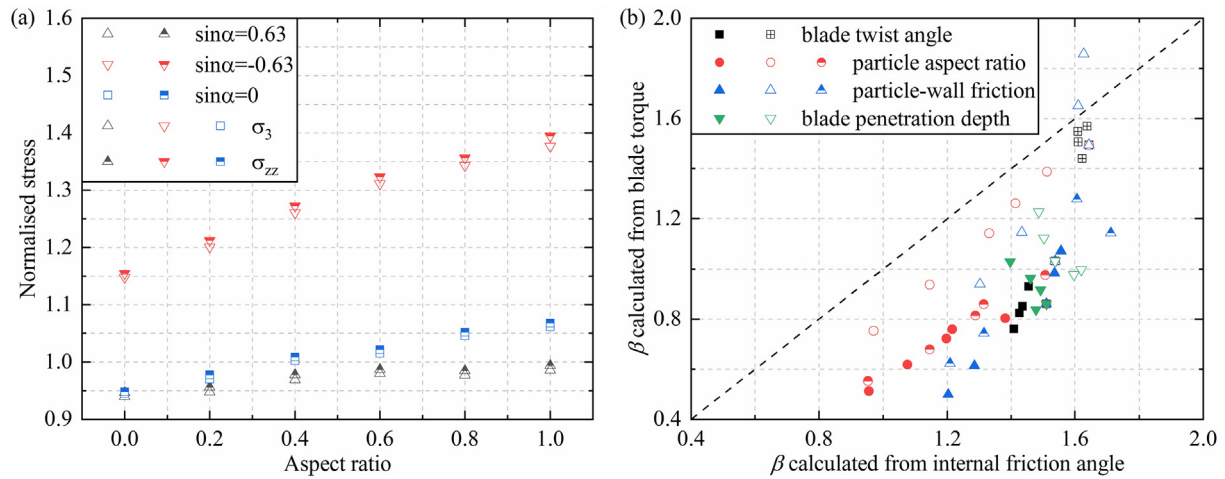


Fig. 13. Comparison between (a) minor principal stress (open symbol) and vertical stress (half-filled symbol) for the shearing surface shown in Fig. 12, and (b) prediction of β from the torque (Eq. (20)) and internal friction angle (Eq. (21)) for 4 kinds of sub-figures in Fig. 10.

experience much smaller stress and they are also far away from the yield point. Therefore, the blade powder rheometer could not be simplified as a rotating cylinder cell with Mohr-Coulomb yield and embedded in the particle bed, and their model has much limits when applying to the blade powder rheometer to predict the internal friction angle of particles from blade torque in dynamic condition at high strain rate. It should be noted that the hypothesis of uniform shear stress on the top/bottom surface in the model of Bruni et al. [13] was later corrected by Tomasetta et al. [15] for large penetration depth, by replacing Janssen analysis with Walker's correction [34,35] (i.e. distribution factor) on σ_{zz} , although no significant improvements on the prediction of blade torque was reported.

Actually, it is difficult to accurately predict the internal friction angle from the measured torque in the rheometer, as the real shear plane is not known, even for the rheometer with a plane blade. Thus, it is more preferable to depict the stress state in the rheometer from the torque at given test conditions. As shown in Fig. 14, the blade torque is indeed cooperative with the shear stress arising in front of the blade, where a linear correlation could be found.

As the blade motion mainly affects the particles close to the blade, whilst particles remote from the blade are essentially stationary, the torque is mainly attributed to the shearing in the region close to the

blade, where large stress prevails. Here, two regions (blue colour) adjacent to two sides of the blade in the moving direction are focused, as shown in Fig. 15, which have the same height (z direction, h) and total length (r direction, $(R-R_s)/2$) of the measurement cell in Fig. 3. The depth (circumferential direction or θ direction) of the regions is in the range of shear band. Considering the actual shearing surface contributing to the blade torque may be larger than the region, an equivalent depth l_e is used based on the shear stress τ in the measurement cell in Fig. 3. The torque is the sum of the contribution of the shear stress on the top/bottom surface (r - θ plane) and lateral inner/outside surface (z - θ plane) of the two regions:

$$T = 2(T_{bot} + T_{top} + T_{inner} + T_{outside}) \quad (22)$$

As the shaft diameter D_s is much smaller than the blade diameter D , the contribution of T_{inner} is much smaller than $T_{outside}$ and is omitted here.

As the shear stress on the top/bottom surfaces (r - θ plane) is not uniform in the radial direction, as shown in Fig. 5, it is assumed to be in a power function of r , given as:

$$\tau_r = \tau_0 \left(\frac{r}{D/2} \right)^m \quad (23)$$

where τ_0 is the shear stress at the tip of the blade on the top/bottom surface; $m = 0$ corresponds to a uniform distribution of shear stress on the surface, and $m = 1$ corresponds to a linear increase of shear stress with r

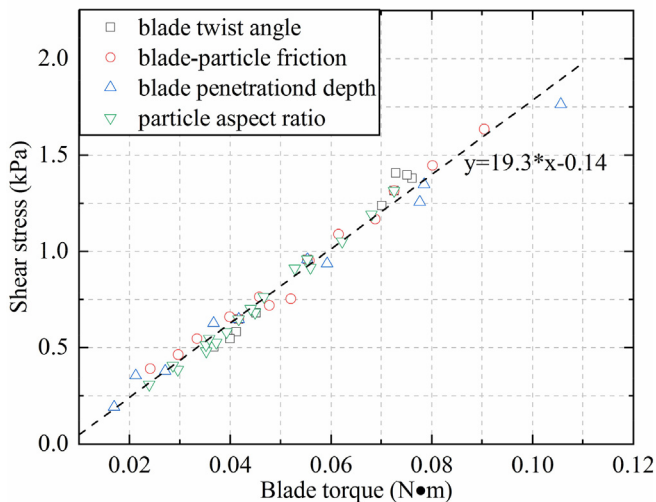


Fig. 14. Linear relationship between shear stress and blade torque.

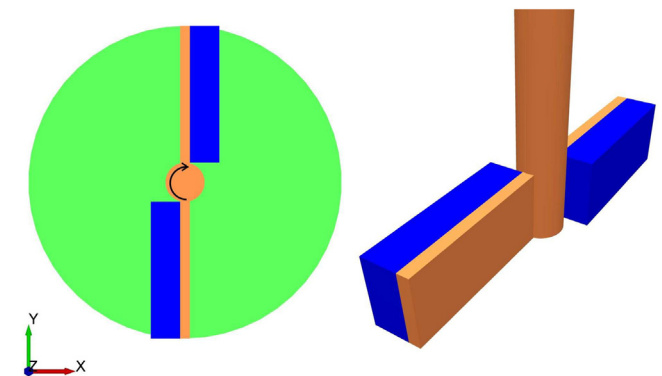


Fig. 15. The region used to estimate the contributions of shear stress to blade torque.

on the surface. The averaged shear stress on the top and bottom surfaces are given as:

$$\tau_a = \frac{\tau_0}{2} \left(1 + \left(\frac{D_s}{D} \right)^m \right) \quad (24)$$

where D_s is the diameter of the shaft. Correspondingly, the shear stress on the lateral outside surface (z - θ plane) is assumed to be uniform and proportional to the shear stress at the blade tip on the top/bottom surface, given as:

$$\tau_{outside} = B\tau_0 \quad (25)$$

where $B \geq 1$ is a constant. T_{bot} is assumed to be equal to T_{top} , given as:

$$T_{bot} = T_{top} = \int_{D_s/2}^{D/2} \tau_r \times l_e dr \times r = \frac{D^2}{4} \frac{l_e \tau_0}{m+2} \left(1 - \left(\frac{D_s}{D} \right)^{m+2} \right) \quad (26)$$

$T_{outside}$ is given as:

$$T_{outside} = \tau_{outside} \cdot l_e h \cdot \frac{D}{2} = \frac{BDh}{2} l_e \tau_0 \quad (27)$$

As $(D_s/D)^2 \approx 0$, and combining Eqs. (26) and (27) into (22), given as:

$$T = D^2 \left(\frac{1}{m+2} + \frac{Bh}{D} \right) l_e \tau_0 \quad (28)$$

Combining Eq. (28) into (24), the averaged shear stress on the top/bottom surface of the consider region is given as:

$$l_e \tau_a = \frac{T}{2D^2} \frac{1 + (D_s/D)^m}{1/(m+2) + Bh/D} \quad (29)$$

where $l_e \tau_a$ could be perceived as the linear density of characteristic shear stress. Fig. 5 shows that the shear stress increases linearly with r for the cases of plane blade and twisted blade with clockwise rotation, i.e. $m = 1$. The major principal stress σ_1 is much larger than σ_2 and σ_3 , σ_{zz} is between σ_2 and σ_3 , and σ_{zz} is larger than hydrostatic pressure γH . Thus, the major principal stress is assumed to in θ direction, while σ_2 and σ_3 are mainly attributed to the compression effect by the blade rotation in θ direction. Therefore, the normal stress on the lateral surface and at the blade tip on the top/bottom surface are assumed to be the same, i.e. $B = 1$. The comparison between $l_e \tau_a$ (predicted from blade torque, Eq. (29)) and τ (analysed in the measurement cell in Section 3.1) is shown in Fig. 16, where only the cases using plane blade

and twisted blade with clockwise rotation are included. A linear trend is found and the slope is 0.013 m, i.e. about $6.5d_v$, which is reasonable as the shear band is usually 3–10 d_v . It is also about 13% of the half arc length of the cylinder surrounding the blade in this work.

4. Conclusions

The rheological behaviour of particles sheared by a rotating blade has been analysed using DEM simulations. The effects of the shape and rotation direction of the blade, blade surface roughness and particle aspect ratio on the particle stress and resistant blade torque have been analysed, and a rheological model between the particle stress and blade torque is proposed. The main results from the present study are summarised as follows:

- 1) In the case of plane blade and clockwise rotation of twisted blade, the shear stress in front of the blade shows a linear increase with the radial position. The rheological behaviour of the particles is affected by the wall friction of the blade, especially for the blade with smooth surface. Both Drucker-Prager and Mohr-Coulomb criterions give high agreement on the prediction of particle rheology in blade rheometer, where non-periodic and fully three-dimensional particle flow is involved.
- 2) The particle stress in front of the blade is sensitive to the rotation direction of the twisted blade. Compared to plane blade, larger shear stress could be obtained in clockwise rotation while the shear stress is much reduced in anti-clockwise rotation. Compared to the stress, the bulk friction coefficient is much less sensitive to the shape and rotation direction of the blade.
- 3) The blade torque is sensitive to blade shape, particle-blade friction coefficient, particle aspect ratio and over-burden depth, which could be depicted from the model proposed this work, i.e. a vertical retaining wall supporting a cohesionless granular material in a passive failure.
- 4) The internal friction angle could not be estimated from blade torque by assuming the shearing surface to a cylinder, i.e. a rotating cylinder cell with Mohr-Coulomb yield and embedded in the particle. The blade torque correlates well with the shear stress in front of the blade, and a mathematic model is proposed to establish the linear relationship between them, where the blade torque is assumed to be mainly attributed to the region where large stress prevails.

Although only free-flowing particles are involved in this work, the proposed models in this work, i.e. Eqs. (14) and (16)–(17) as well as Eq. (29), are still valid for the rheological behaviour of cohesive particles in blade rheometer, as the particle properties are not specified during the derivation. The implications of inter-particle cohesion on the results could be inferred to be the variation of bulk particle friction and wall friction in Eq. (14) or Eq. (16) as well as linear density of shear stress in Eq. (29), resulting in the changes of blade torque which are intuitively expected. However, the rheological behaviour of cohesive particles at high shear strain rate, which was recently reviewed by Ghadiri et al. [3], still needs further investigation as the role of inter-particle cohesion in powder rheology is far from comprehensive understanding.

Declaration of Competing Interest

The authors declare that they have no known competing financial interests or personal relationships that could have appeared to influence the work reported in this paper.

Acknowledgments

The authors are grateful to the National Natural Science Foundation of China (Grant No. 51806099) and Start-up Foundation for Introducing Talent of Nanjing Tech University (Grant No. 39802120) for the financial support of this work. The authors are also thankful to Professor Mojtaba

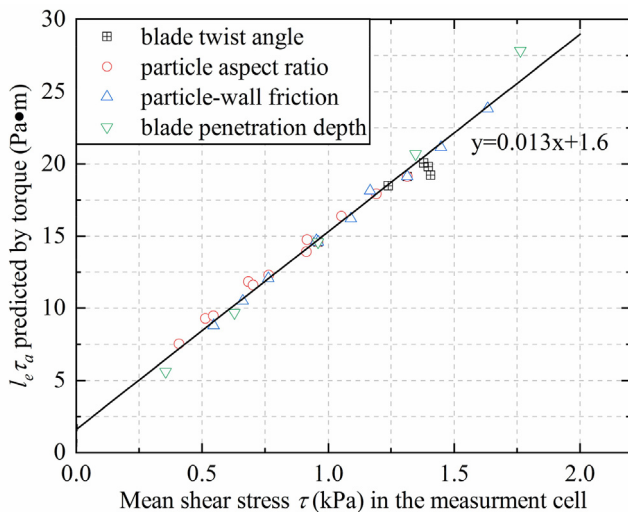


Fig. 16. Comparison between $l_e \tau_a$ and τ for the cases using plane blade and twisted blade with clockwise rotation.

Ghadiri, University of Leeds, for the inspiration and encouragement on this work, and Professor Yueshe Wang, Xi'an Jiaotong University, for the providing of the software resources.

References

- [1] D. Schulze, *Powders and Bulk Solids Behavior, Characterization, Storage and Flow*, Springer, Verlag Berlin Heidelberg, 2007.
- [2] A. Castellanos, J.M. Valverde, M.A.S. Quintanilla, The Sevilla powder tester: a tool for characterizing the physical properties of fine cohesive powders at very small consolidations, *KONA Powd. Particle J.* 22 (2004) 66–81.
- [3] M. Ghadiri, M. Pasha, W. Nan, C. Hare, V. Vivacqua, U. Zafar, S. Nezamabadi, A. Lopez, M. Pasha, S. Nadimi, Cohesive powder flow: trends and challenges in characterisation and analysis, *KONA Powd. Particle J.* 37 (2020) 3–18.
- [4] G.I. Tardos, S. McNamara, I. Talu, Slow and intermediate flow of a frictional bulk powder in the Couette geometry, *Powder Technol.* 131 (2003) 23–39.
- [5] M.K. Langroudi, S. Turek, A. Ouazzi, G.I. Tardos, An investigation of frictional and collisional powder flows using a unified constitutive equation, *Powder Technol.* 197 (2010) 91–101.
- [6] V. Vidyapati, M. Kheiripour Langroudi, J. Sun, S. Sundaresan, G.I. Tardos, S. Subramaniam, Experimental and computational studies of dense granular flow: transition from quasi-static to intermediate regime in a Couette shear device, *Powder Technol.* 220 (2012) 7–14.
- [7] M. Kheiripour Langroudi, P.R. Mort, G.I. Tardos, Study of powder flow patterns in a Couette cell with axial flow using tracers and solid fraction measurements, *Granul. Matter* 13 (2011) 541–552.
- [8] K.J. Gutam, V. Mehandia, P.R. Nott, Rheometry of granular materials in cylindrical Couette cells: anomalous stress caused by gravity and shear, *Phys. Fluids* 25 (2013), 070602.
- [9] V.S. Kumar, T. Murthy, P.R. Nott, Rheometry of dense granular materials: the crucial effects of gravity and confining walls, *Aip Conf. Proc.* 1542 (2013) 49–51.
- [10] M. Lupo, D. Schütz, E. Riedl, D. Barletta, M. Poletto, Assessment of a powder rheometer equipped with a cylindrical impeller for the measurement of powder flow properties at low consolidation, *Powder Technol.* 357 (2019) 281–290.
- [11] R. Freeman, Measuring the flow properties of consolidated, conditioned and aerated powders – a comparative study using a powder rheometer and a rotational shear cell, *Powder Technol.* 174 (2007) 25–33.
- [12] H. Salehi, D. Sofia, D. Schütz, D. Barletta, M. Poletto, Experiments and simulation of torque in Anton Paar powder cell, *Part. Sci. Technol.* 36 (2018) 501–512.
- [13] G. Bruni, D. Barletta, M. Poletto, P. Lettieri, A rheological model for the flowability of aerated fine powders, *Chem. Eng. Sci.* 62 (2007) 397–407.
- [14] G. Bruni, A. Colafigli, P. Lettieri, T. Elson, Torque measurements in aerated powders using a mechanically stirred fluidized bed Rheometer (msFBR), *Chem. Eng. Res. Des.* 83 (2005) 1311–1318.
- [15] I. Tomasetta, D. Barletta, P. Lettieri, M. Poletto, The measurement of powder flow properties with a mechanically stirred aerated bed, *Chem. Eng. Sci.* 69 (2012) 373–381.
- [16] H. Salehi, D. Barletta, M. Poletto, D. Schütz, R. Romirer, On the use of a powder rheometer to characterize the powder flowability at low consolidation with torque resistances, *AIChE J.* 63 (2017) 4788–4798.
- [17] C. Hare, U. Zafar, M. Ghadiri, T. Freeman, J. Clayton, M.J. Murtagh, Analysis of the dynamics of the FT4 powder rheometer, *Powder Technol.* 285 (2015) 123–127.
- [18] W. Nan, V. Vivacqua, M. Ghadiri, Y. Wang, Numerical analysis of air effect on the powder flow dynamics in the FT4 powder Rheometer, *Powd. Grains* 2017 France (2017) 03036.
- [19] W. Nan, M. Ghadiri, Y. Wang, Analysis of powder rheometry of FT4: effect of particle shape, *Chem. Eng. Sci.* 173 (2017) 374–383.
- [20] W. Nan, M. Ghadiri, Y. Wang, Analysis of powder rheometry of FT4: effect of air flow, *Chem. Eng. Sci.* 162 (2017) 141–151.
- [21] V. Vivacqua, A. López, R. Hammond, M. Ghadiri, DEM analysis of the effect of particle shape, cohesion and strain rate on powder rheometry, *Powder Technol.* 342 (2019) 653–663.
- [22] P.A. Cundall, O.D.L. Strack, A discrete numerical model for granular assemblies, *Géotechnique* 29 (1979) 47–65.
- [23] C. Thornton, *Granular Dynamics, Contact Mechanics and Particle System Simulations*, Springer, New York, 2015.
- [24] J.F. Favier, M.H. Abbaspour-Fard, M. Kremmer, A.O. Raji, Shape representation of axisymmetrical, non-spherical particles in discrete element simulation using multi-element model particles, *Eng. Comput.* 16 (1999) 467–480.
- [25] Z. Grof, C.M. Schoellhammer, P. Rajniak, F. Stepanek, Computational and experimental investigation of needle-shaped crystal breakage, *Int. J. Pharm.* 407 (2011) 12–20.
- [26] Z. Grof, M. Kohout, F. Stepanek, Multi-scale simulation of needle-shaped particle breakage under uniaxial compaction, *Chem. Eng. Sci.* 62 (2007) 1418–1429.
- [27] W.G. Nan, Y.S. Wang, Y. Ge, J.Z. Wang, Effect of shape parameters of fiber on the packing structure, *Powder Technol.* 261 (2014) 210–218.
- [28] W. Nan, Y. Wang, H. Sun, Experimental investigation on the packed bed of rodlike particles, *Adv. Powder Technol.* 30 (2019) 2541–2547.
- [29] B. Remy, J.G. Khinast, B.J. Glasser, Discrete element simulation of free flowing grains in a four-bladed mixer, *AIChE J.* 55 (2009) 2035–2048.
- [30] B. Remy, J.G. Khinast, B.J. Glasser, Polydisperse granular flows in a bladed mixer: experiments and simulations of cohesionless spheres, *Chem. Eng. Sci.* 66 (2011) 1811–1824.
- [31] R.K. K. N.P. R. S. S., *An Introduction to Granular Flow*, Cambridge University Press, New York, 2008.
- [32] N.R. M., *Statics and Kinematics of Granular Materials*, Cambridge University Press, 2005.
- [33] D.F. Bagster, J. Bridgwater, The flow of granular material over a moving blade, *Powder Technol.* 3 (1969) 323–338.
- [34] D.M. Walker, An approximate theory for pressures and arching in hoppers, *Chem. Eng. Sci.* 21 (1966) 975–997.
- [35] J.K. Walters, A theoretical analysis of stresses in silos with vertical walls, *Chem. Eng. Sci.* 28 (1973) 13–21.